Batteries & Supercaps

Research Article
doi.org/10.1002/batt.202300580

Chemistry Europe
European Chemical
Societies Publishing

www.batteries-supercaps.org

Interphase design of LiNi$_{0.6}$Mn$_{0.2}$Co$_{0.2}$O$_2$ as positive active material for lithium ion batteries *via* Al$_2$O$_3$ coatings using magnetron sputtering for improved performance and stability

Atif Javed,[a, b] Ardavan Makvandi,[c] Feleke Demelash,[a] Egy Adhitama,[a, b] Bastian Heidrich,[a] Martin Peterlechner,[c] Gerhard Wilde,[c] Martin Winter,[a, d] and Markus Börner*[a]

LiNi$_x$Mn$_y$Co$_z$O$_2$ ($x+y+z=1$) is one of the most present and versatile positive active materials for lithium ion batteries due to comparatively high specific capacity and high operating potential. However, NMC materials are prone to various degradation effects including moisture uptake, formation of impurities at the particle surface and transition metal dissolution during charge/discharge cycling and/or at elevated temperatures. Beyond that, cation mixing can lead to phase transformation, oxygen evolution, particle cracking and particle disintegration. Therefore, an alumina coating was applied and optimized as protective interphase on LiNi$_{0.6}$Mn$_{0.2}$Co$_{0.2}$O$_2$ (NMC622) powders, using a specifically in-house developed RF-

magnetron sputtering technique. The alumina coated NMC622 showed a 13% improvement in capacity retention after 200 charge/discharge cycles in lab-scale cells, compared to pristine uncoated NMC622. Using electrochemical impedance spectroscopy, the interfacial/interphasial resistance of pristine and alumina coated NCM622 based electrodes were explored to study the impact of the coating on lithium ion transport. Furthermore, the structural and thermal stability of cyclic aged NMC622 were analyzed *via* TEM, EELS and TGA. Therein, alumina coated samples demonstrated enhanced thermal stability, less structural degradation, and reduced particle cracking.

1. Introduction

Lithium ion batteries (LIBs) have been explored and developed extensively as dominant energy storage systems for portable electronics to large-scale applications, including electric vehicles since their discovery in the 1970ies and 1980ies and first commercialization by Sony in 1991.[1] Still today, LIBs face many challenges regarding lifetime, safety and costs. In first-gener-

ation commercial LIBs, LiCoO$_2$ was widely used as positive active material (cathode) due to its comparatively good electrochemical performance, ease of processing and high volumetric capacity but had to face serious disadvantages such as high toxicity, costs and safety issues which led researchers to focus on alternative layered materials with reduced amounts of cobalt.[2–4] Three-component layered transition metals oxides LiNi$_x$Mn$_y$Co$_z$O$_2$ (NMC, $x+y+z=1$) received a lot of attention as cathode active material (CAM) as they exhibit improved electrochemical performance depending on the relative composition of Ni, Mn and Co. High Ni content in NMC contributes to higher specific capacity (discharge capacity of 200 mAh g^{-1} for $x=0.8$) at the expense of safety. High Mn content improves structural stability at the expense of capacity and high cobalt content improves structural stability and reduce Li/Ni mixing but has high cost and increased toxicity.[5–8]

NMC stoichiometries with nickel contents up to 80%, like LiNi$_{0.6}$Mn$_{0.2}$Co$_{0.2}$O$_2$ (NMC622) and LiNi$_{0.8}$Mn$_{0.1}$Co$_{0.1}$O$_2$ (NMC811) are commercialized as state-of-the-art CAM and used in various stationary and mobile battery applications, e.g., electric vehicles (EVs). Therein, the continuously evolving EV market demands LIB active materials enabling high specific energy (Wh kg^{-1}) and energy density (Wh L^{-1}) on cell level.[6,9] NMCs with nickel contents as high as $x \geq 0.9$ were reported to have high specific capacity as increasing the amount of nickel increases the specific capacity for the same voltage window but in turn, decreases the Mn and Co contents leading to lower thermal and electrochemical stability.[10–12] Beyond that, NMC with high nickel content suffers from cation mixing of Li$^+$ (0.076 nm) and Ni^{2+} (0.069 nm) because of very similar ionic radii, which in turn

[a] A. Javed, F. Demelash, E. Adhitama, B. Heidrich, M. Winter, M. Börner
MEET Battery Research Center
Corrensstr. 46, 48149 Münster, Germany
E-mail: markus.boerner@uni-muenster.de

[b] A. Javed, E. Adhitama
University of Münster
International Graduate School for Battery Chemistry Characterization
Analysis Recycling and Application (BACCARA)
Corrensstr. 40, 48149 Münster, Germany

[c] A. Makvandi, M. Peterlechner, G. Wilde
University of Münster
Institute of Materials Physics
Wilhelm-Klemm-Str.10, 48149, Münster, Germany

[d] M. Winter
Forschungszentrum Jülich GmbH
Helmholtz Institute Münster (IEK-12)
Corrensstr. 46, 48149 Münster, Germany

results in capacity loss and structural degradation.[13] Apart from structural instabilities, surface impurities can form during the synthesis of NMC due to the addition of extra Li with precursors to compensate Li loss during calcination at high temperatures, leading to the formation of LiOH, Li_2CO_3 and Li_2O residues on the surface of NMC particles as surface contaminants.[12] These contaminations can react with different electrolyte components to form decomposition products at the NMC surface, the so-called cathode electrolyte interphase (CEI), associated with an increase in cell impedance.[14] Apart from surface impurities from synthesis, NMCs are also prone to moisture uptake and adsorbed water residues can dissolve into the electrolyte, accelerating the decomposition of electrolyte components and potentially resulting in HF production, which is corrosive in nature, promoting transition metal (*TM*) dissolution and leading to the formation of resistive CEI species.[2,15]

In the literature on CAM, surface coatings proved to be a promising approach to improve the electrochemical performance, thermal properties and surface structural stability of CAM.[16] Ideally, protective coatings are thin and homogeneous, preferably ionically conductive, have good electrochemical and thermal stability and are overall cost-effective.[17] In literature, a wide range of coatings were explored, ranging from metallic oxides (Al_2O_3 ,[18] SiO_2, TiO_2,[19] WO_3,[5] ZrO_2[20]), phosphates (Li_3PO_4[21] and $AlPO_4$[22]) and fluorides (AlF_3[23] and LiF[24]) to conductive polymer-based coatings (polypyrrole and polyaniline)[25] each of them having their own advantages and disadvantages. Protective coatings and interphases act, among others as a physical barrier between active material and electrolyte, mitigating parasitic side reactions and thus preventing the formation of decomposition products and subsequently enhancing the overall electrochemical performance. Coatings like SiO_2 and Al_2O_3 act as HF scavenger by preventing the chemical attack towards the CAM, which prevents transition metal dissolution to a great extent.[26] Some electronically and ionically conductive coatings ensure fast Li^+ mobility through the coating layer resulting in the reduction of charge transfer resistance R_{ct}, which enables fast charging and discharging.[21] However, when the coatings are electronically conductive, they could enhance CEI formation and growth by taking up electrons for oxidation reactions.

Various coating processes/strategies were developed and reported depending on the desired properties and electrochemical goals. Coating techniques can be generally classified into three categories: (i) wet chemical techniques, (ii) dry coating/mechano-fusion and (iii) gas phase deposition.[17] In the wet chemical route, sol-gel and hydrothermal-based coating techniques are commonly used.[27,28] Therein sol-gel processing benefits from simplicity, scalability and can be applied to various coating materials. However, to evaporate water or other solvents, an additional drying step is needed.[29] The hydrothermal coating process utilizes high pressure in specifically designed reactors enabling homogenous coatings with good control over thickness and stoichiometry. However, this process is not suitable for large scale production of coated materials as it uses expensive precursors, has low yield and an additional heating step is employed to process solvents.[30] Due to

inexpensive precursors, ease of processing and upscaling the mechano-fusion route is the most viable option for commercialization as it simply involves mixing cathode active material with coating material/precursor using a ball mill and subsequent heat treatment of mixed materials. This coating process is simple, cost-effective, can be used at large scale and can be applied for a lot of different coatings materials.[31] However, with this technique, the homogeneity and thickness of the coating are very difficult to control precisely.[32] Alternatively, coating processes like physical vapor deposition (PVD), chemical vapor deposition (CVD) and atomic layer deposition (ALD) are based on gas phase processes. These deposition techniques produce homogenous coatings with very good control over thickness. Beyond that, no additional heating step is needed in these solvent-free coating processes. However, deposition-based coating techniques are commonly applied on already prepared electrode sheets, which results in partial protection as particles underneath the surface are mostly unprotected and prone to degradation reactions.[33]

In this study, a novel coating technique based on reactive magnetron sputtering was applied for the first time on CAM powders. Coatings obtained using this technique showed high homogeneity with good surface coverage and control over thickness. In reactive sputtering, the reactive gas is introduced into the sputtering chamber to obtain coatings composed of oxides or nitrides, depending on the reactive gas used. In this study, O_2 was used as a reactive gas to deposit alumina (Al_2O_3) coating in combination with an aluminum (Al) target. A purpose-built magnetron sputtering device was used to do coatings on powders as it consists of a sample holder bowl that is continuously rotating and shaking throughout the sputtering process, and with the help of two brushes and a roller, the powder is continuously mixed and pressed in order to prevent agglomeration of powders and obtain a homogenous coating on all particles. The device setup and principle of coating are shown in Figure 1.

Al_2O_3 coatings with different thicknesses were deposited on NMC622 particles using a magnetron sputtering device to enhance the electrochemical and safety performance. Uniformity and homogeneity of coatings were analyzed using scanning electron microscopy (SEM), energy dispersive X-ray spectroscopy (EDX) and transmission electron microscopy (TEM). Electrochemical characterization was performed with regards to rate capability, long term cycling stability and interfacial resistances. Post-mortem analysis after 200 cycles was performed using (high – resolution) HR-TEM, nano-beam electron diffraction (NBD), electron energy-loss spectroscopy (EELS) and thermo gravimetric analysis (TGA) to understand the role of the alumina coating on NMC622 in performance enhancement.
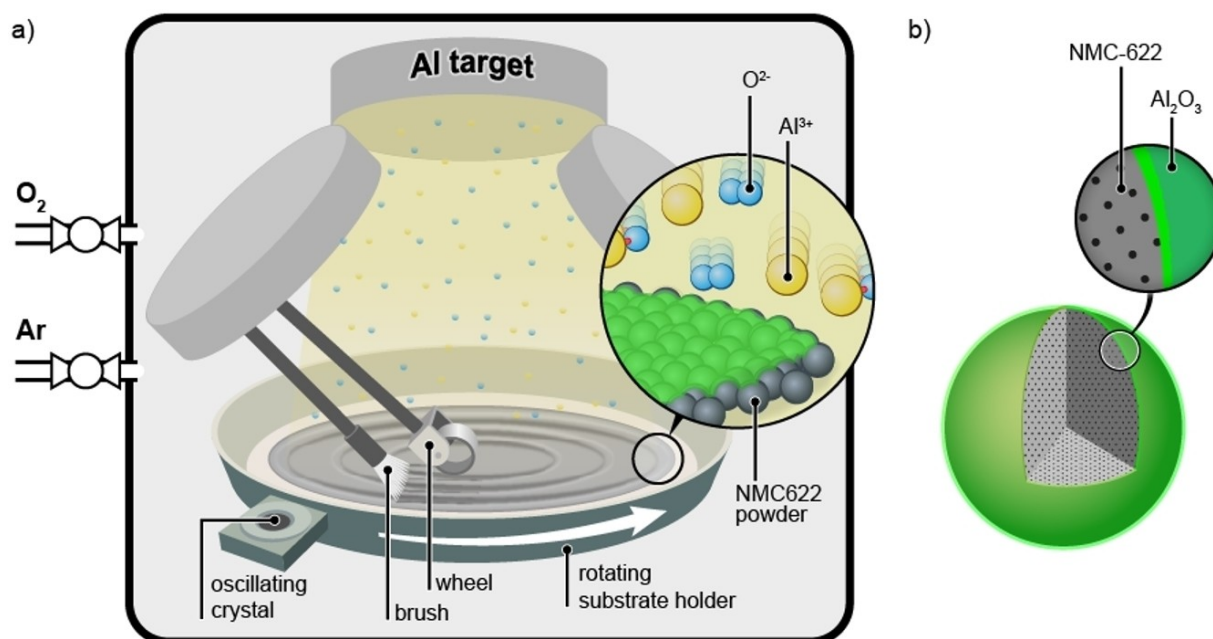
Figure 1. Schematic illustration of a) alumina coating process and device setup b) NMC622 particles coated with alumina.

2. Results and discussion

2.1. Surface morphology and characterization of alumina coated NMC622

In order to develop an alumina based interphase design for enhanced performance, *i.e.* cycle life, rate performance and safety of NMC622 based electrodes, four powder samples were prepared and investigated: a pristine, completely uncoated NMC622 as reference and alumina coated NMC622 with three different calculated layer thicknesses (5 nm, 7 nm and 10 nm) as

surface modified samples. The morphology of the pristine and 10 nm alumina coated NMC622 particles was analyzed using SEM (Figure 2a and b). Therein, the particle surface morphology was not notably affected by the coating process. Surface coverage of the alumina-coated NMC particles was initially analyzed by performing EDX mapping experiments, as shown in Figure 2 (c, d, e, and f). EDX elemental mapping displays the expected uniform distribution of Al and Ni (representative for *TMs*) over the entire surface of NMC particles, confirming the presence of a coating layer with good surface coverage. In addition to the SEM/EDX results, a detailed analysis using HR-
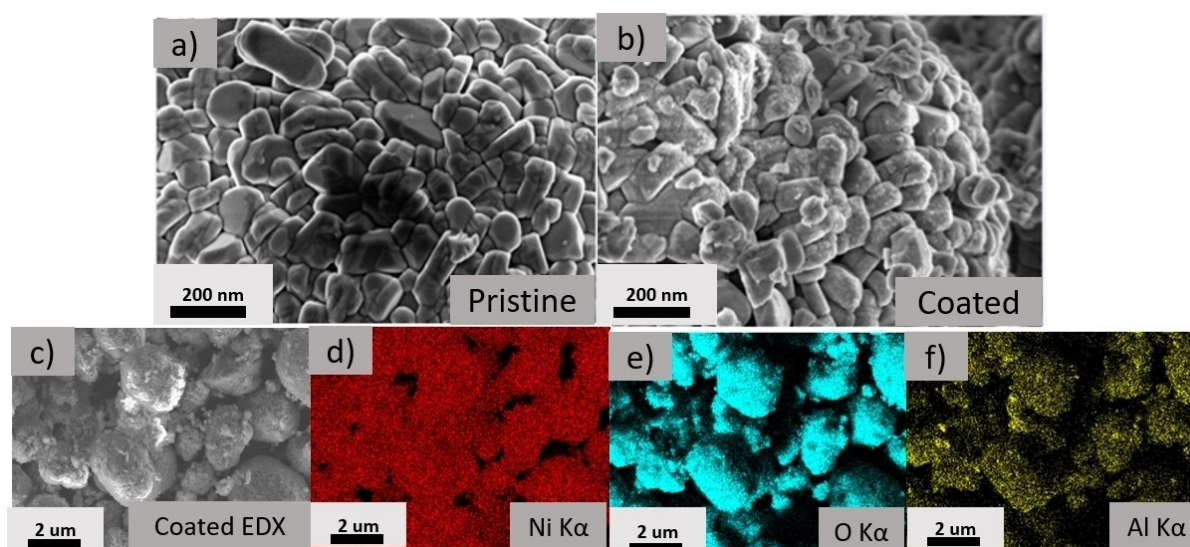

Figure 2. SEM micrographs of a) pristine, b) 10 nm alumina coated NMC622 and c–f) color coded EDX maps showing elemental compositions of Ni, O and Al on alumina coated NMC622 particles.

Batteries & Supercaps

Research Article
doi.org/10.1002/batt.202300580

Chemistry Europe
European Chemical
Societies Publishing

TEM an EDX-STEM was carried out to further confirm the homogeneity of coating.

In addition to the SEM/EDX measurements, a detailed analysis was carried out to determine the homogeneity and surface coverage of NMC622 with alumina coating. EDX-STEM elemental mappings and line-profile analysis were performed. Figure 3 (a and d) shows HAADF-STEM images of the pristine and 10 nm alumina coated NMC622 primary particles with yellow arrows indicating the line across which the EDX line-profiles were obtained. Figure 3 (b and f) shows the homogenous distribution of Ni (as a representative of all *TMs*) at the surface of both pristine and alumina coated NMC622 respectively. Figure 3e) shows EDX elemental spectra of Al, which confirms the presence of an alumina coating layer with good surface coverage as the mapping from the edges of NMC particle show a uniform and continuous signal of Al. The EDX line-profile from the pristine NMC622 shows a constant signal from *TMs* throughout the measurement, and the intensity of the oxygen signal is higher at the particle edges because of the formation of surface impurities in the form of oxides during synthesis of NMC and during storage. Furthermore, for the 10 nm alumina coated NMC622, the *TMs* signal starts at lower values at the surface and gradually increases into the bulk where it remains constant, indicating the presence of a surface coating layer. To confirm the coating presence by a complimentary method, XPS was performed, which shows a signature Al 2p signal in only alumina coated NMC622, where the peak intensity increases with increasing coating thickness (Figure S1a of supporting information). The EDX elemental mapping and line-profile show a homogeneous distribution of Ni, Mn, and Co as shown in Figure S1(b–e) of the supporting information.

Moreover, the high concentration of oxygen and Al at the electrode surface, as shown in the EDX-STEM elemental mapping and line-profile, confirm the presence of an alumina coating layer with a high coverage rate. Figure S2 shows the HR-TEM and corresponding FFT pattern of the alumina coating, confirming its crystallinity.

2.2. Electrochemical characterization

In order to investigate the impact of alumina coating-based interphase design on the electrochemical performance, such as rate capability and charge/discharge cycling stability were evaluated. Figure 4(a) shows a comparison of the rate capability of electrodes based on pristine and alumina coated NMC622 with the theoretically adjusted thickness of 5, 7 and 10 nm. The coating thicknesses correspond to 0.0046, 0.0067 and 0.0094 wt%, respectively, of the active material weight and was therefore considered negligible with regard to active material mass and specific capacity determined for rate capability and long term charge/discharge cycling tests. Pristine NMC622 shows a higher rate capability (at all C-rates) compared to alumina coated NMC622 based electrodes, presumably due to the introduced low ionic conductivity of the alumina coating, which impedes Li$^+$ transport through the coating layer. The alumina coated NMC622 based electrodes exhibit similar rate capabilities up to 2C. Only at 5C, cells based on electrodes with 5 nm alumina coated NMC622 show a higher discharge capacity compared to 7 and 10 nm alumina coatings. For coated materials, typically different factors influence the C-rate performance such as coating thickness, porosity of the coatings,
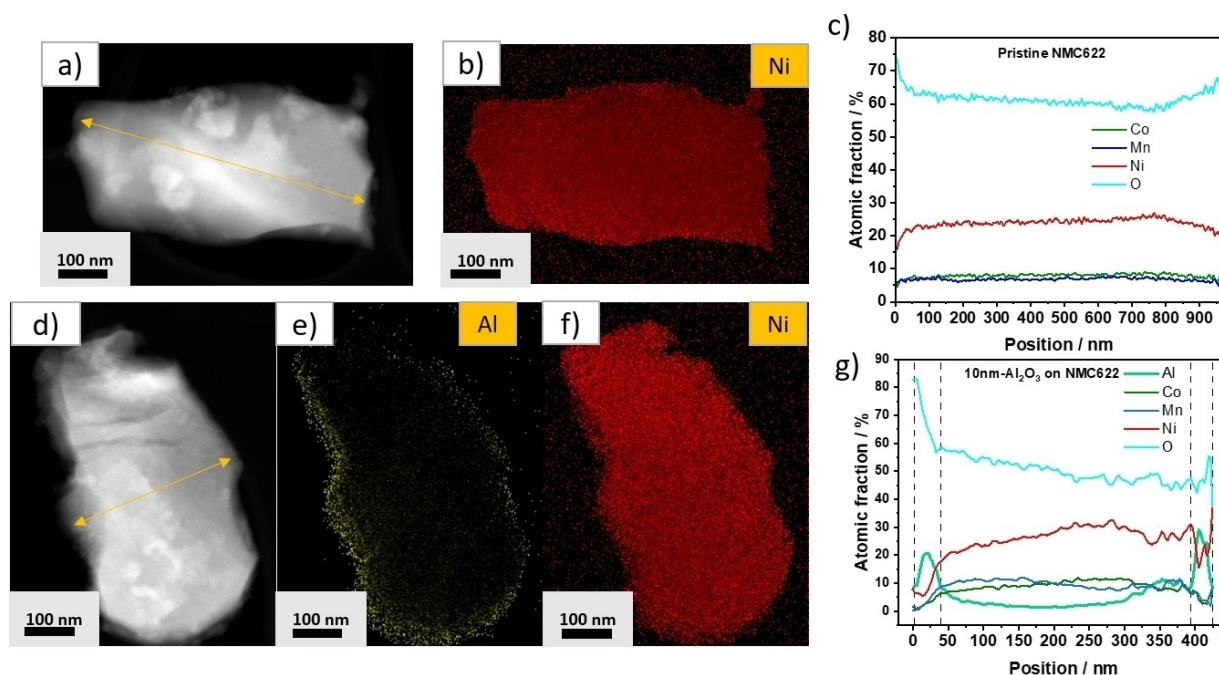

Figure 3. HAADF-STEM images of a) pristine NMC622 d) 10 nm alumina coated NMC622, EDX-STEM elemental mapping b) Ni-distribution on pristine NMC622 (e and f) Ni and Al-distribution on 10 nm alumina coated NMC622 and EDX line-profile of c) pristine and g) 10 nm alumina coated NMC622 (measured across the yellow line highlighted in a and d).
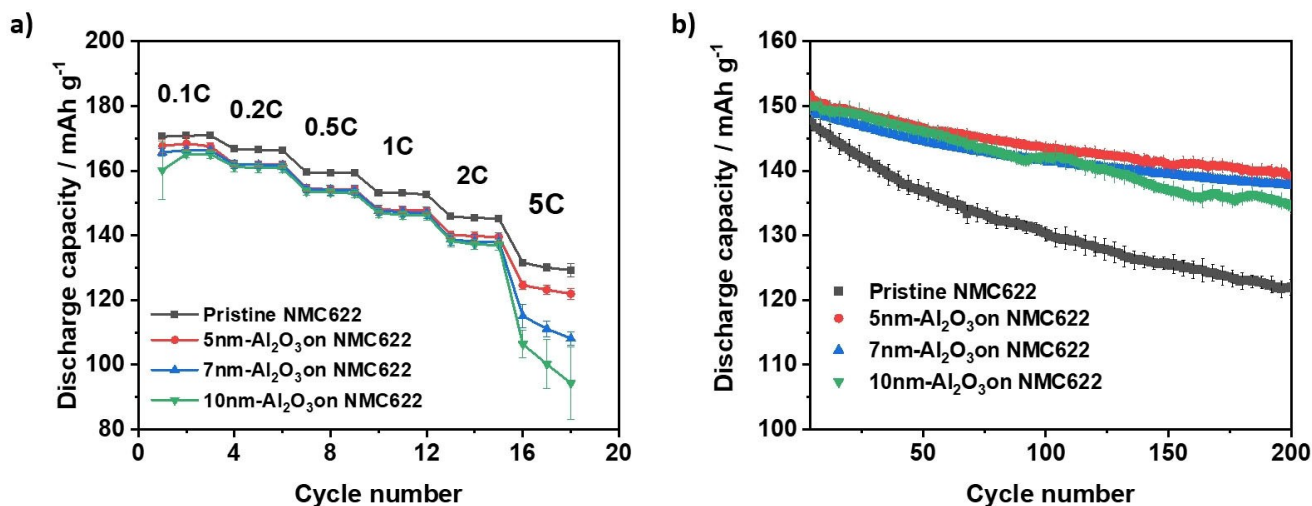
Batteries & Supercaps

Research Article
doi.org/10.1002/batt.202300580

Chemistry
Europe
European Chemical
Societies Publishing

Figure 4. Comparison of a) rate capability in two electrode cells of various NMC622 positive electrodes *versus* lithium metal as negative electrode applying symmetric cycling at different C-rates and b) long term charge/discharge cycling performance at 1C of pristine, 5, 7, and 10 nm alumina NMC622 based positive electrodes in cells *versus* graphite as negative electrode.

and homogeneity. A very thin coating layer (<5 nm) cannot effectively protect CAM from the electrolyte attack and a thick coating layer can increase the resistance of Li^+ transport, causing non-uniform (de−)lithiation and mechanical stress. An appropriate coating thickness can effectively protect the CAM and does not hinder Li^+ transport at the same time. The porosity of the coating layer reduces the insulating effect of coating material by reducing the effective coating layer thickness. Improved rate performance of 5 nm alumina coated NMC622 amongst other alumina coated NMC622 was attributed to the uniform coating with appropriate thickness resulting in the formation of an effective CEI with enhanced ionic conductivity, which facilitates the Li^+ transport at elevated C-rates (rate capability decreasing with increasing coating thickness). It is worth noting that at high current densities, the discharge capacity decreases due to the limited transport of Li^+ in the porous composite electrode and within the CAM particles, as seen for all cells at 2C and 5C.[34] An additional factor that facilitates the rate capability is the nature of active material coating. When coatings are ionically conductive, they will facilitate the Li^+ transport through the coating layer and hence perform better at elevated C-rates. However, metal oxide-based coatings impede the Li^+ mobility towards the CAM surface, reducing the power density and discharge capacity at increasing thicknesses.[19] Despite this behavior in this study, several reports using alternative coating techniques were published showing an improvement in the rate capability for alumina coated NMC622 due to the formation of mixed Al_2O_3/ $LiAlO_2$ coating layer during the wet chemical coating process (which involves annealing at higher temperatures) or some attributed it to an overall decrease of the cell impedance for coated materials.[5,35]

To investigate the impact of alumina coating on cycling stability, electrodes based on pristine, 5, 7 and 10 nm alumina coated NMC622 were cycled in a NMC622||graphite cell setup. In Figure 4b) alumina coated samples showed an enhanced

cycling performance with improved capacity retention (94% for 5 nm, 92% for 7 nm and 90% for 10 nm alumina NMC622) as compared to the pristine sample (81%) after the same number of charge/discharge cycles. Herein, it has to be considered that the loss of lithium inventory due to irreversible side reactions directly affects the specific capacity as the lithium reservoir is limited by NMC cathode, which was not the case for rate capability tests with an almost unlimited lithium reservoir. Alumina coating forms a protective layer that prevents direct contact between the electrolyte and CAM hence mitigating the degradation effects such as HF production leading to *TMs* dissolution and structural instability as well as deposition of decomposition products on electrode surface like LiF, which is highly resistive to the Li^+ transport leading to severe capacity fade as shown in Figure 4(b) for uncoated sample.[36,37] *TMs* dissolution from the CAM surface leads to lattice damage and structural degradation, which initiate cracks in the secondary cathode particles and cause particle disintegration. Alumina coating protected the CAM against electrolyte attack, phase transformation, *TMs* dissolution, surface reconstruction, and particle cracking, which resulted in a substantial improvement of capacity retention (more than 90% for all coated samples).[26]

Figure 5 shows the voltage *vs.* discharge capacity profile and corresponding differential capacity plots *vs.* voltage of electrodes based on pristine and 5 nm alumina coated NMC622 after the 5th, 50th, 100th and 200th cycle. The initial discharge capacity and Coulombic efficiency for pristine (158 mAh g^{-1} and 70% for 1st cycle) and 5 nm alumina coated NMC622 (176 mAh g^{-1} and 85% for 1st cycle) is not discussed here due to irreversible reactions occurring during the first 3 formation cycles. The discharge capacity after the formation procedure is slightly lower for the coated NMC622 (148 mAh g^{-1}) compared to the pristine NMC622 (150 mAh g^{-1}) due to the lack of electronic conductivity of Al_2O_3 coating and no voltage drop was observed in the voltage *vs.* capacity profiles for both, pristine and 5 nm alumina coated NMC622, with increasing
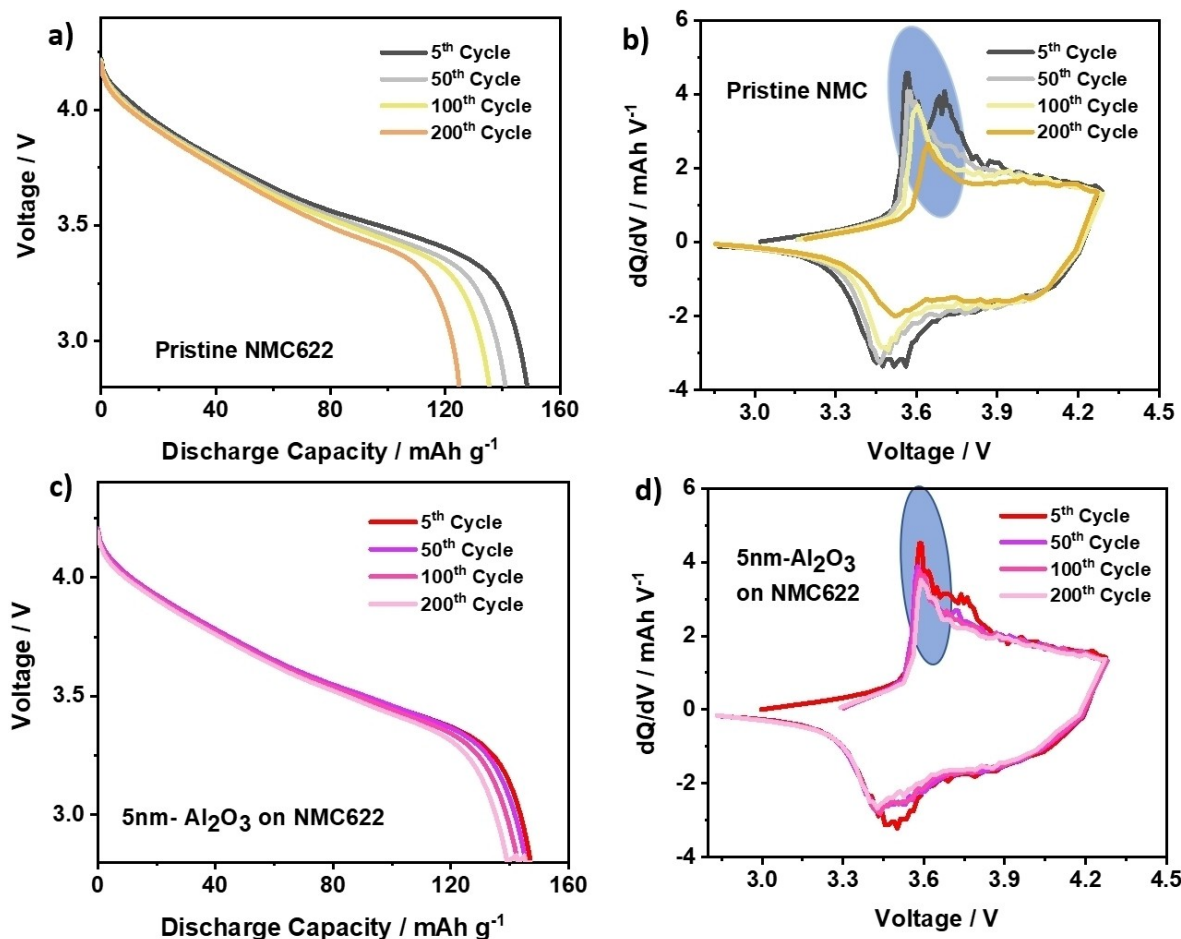
Batteries & Supercaps

Research Article
doi.org/10.1002/batt.202300580

Chemistry Europe
European Chemical
Societies Publishing

Figure 5. Voltage *vs.* capacity profiles of electrodes based on a) pristine NMC622, b) 5 nm alumina coated NMC622 and (c, d) corresponding differential capacity *vs.* voltage plots at 1C for long term cycling after 5th, 50th, 100th, and 200th cycles in cells with various NMC622 positive electrodes *versus* a graphite negative electrode.

number of charge/discharge cycles (Figure 5a and c). However, the slight decrease in initial capacity for the coated sample is compensated with improved cycling stability even after 200 cycles, where 5 nm alumina coated NMC622 showed 94% capacity retention compared to 81% for pristine NMC622. Improved cycling stability for the coated samples was attributed to inhibiting the side reactions by covering the surface of reactive NMC622, suppressing electrolyte decomposition and structural transformation (layered-spinel-rock-salt), and, thus, preventing the formation of a resistive and ineffective CEI/SEI. These results are further supported by the differential capacity (dQ/dV) *vs.* voltage plots shown in Figure 5 (b and d). It is determined that for pristine NMC622 the oxidation reactions shift to higher values while the reduction reaction shift to lower values, which indicates an increase in cell resistance for the pristine sample, as shown by a colored circle in Figure 5b). Apart from the shift, the redox peaks progressively broaden with an increasing number of cycles, indicating deterioration of the cathode/electrolyte interface and the deposition of decomposition products, resulting in the formation of a highly resistive CEI, negatively affecting the cycling performance. For alumina coated NMC622, the shift in the redox peaks is not detected

which proves the effectiveness of the coating in reducing the degradation effects, stabilization of the cathode/electrolyte interface, suppressing the phase transformation and hence improving the electrochemical performance.[38] Sharp differential capacity *vs.* voltage peaks for the coated sample indicate the formation of a stable CEI and better preserved Li$^+$ transport pathways after 200 cycles. Whereas, peak broadening and reduced intensity for the pristine NMC622 with an increasing number of charge/discharge cycles indicates a resistive CEI due to the enhanced electrolyte decomposition, loss of active lithium, and increase in cell resistance, which is responsible for the severe capacity fading observed during 200 charge/discharge cycles.

To further elucidate the effect of the alumina coating, EIS was performed which gives deeper insight into the cell impedance compared to the dQ/dV *vs.* voltage analysis. EIS after formation and after 200 charge/discharge cycles was performed as shown in Figure 6 (a and b). EIS analysis gives information about different processes. In a Nyquist plot, a semicircle at high frequency (High frequencies at low Z' values) represents CEI resistance and denoted as R$_{CEI}$, the semicircle in medium to low frequency range represents the charge transfer
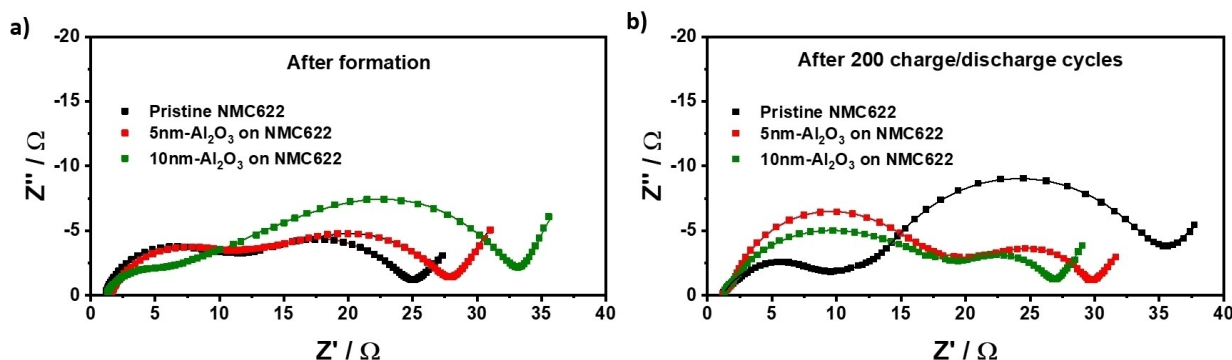
Figure 6. Nyquist plots from electrochemical impedance spectroscopy measured at 50 % state of charge for electrodes based on pristine, 5 nm and 10 nm alumina coated NMC622 a) after formation and b) after 200 charge/discharge cycles at 1C.

resistance (R_{ct}) which is the resistance at the outermost surface of NMC particles. Finally, the low-frequency region represents impedance for lithium diffusion through the solid phase of active material.[39,40] Figure 6a) shows the Nyquist plots of pristine and alumina coated NMC622 after formation. Cells based on pristine NMC622 show smaller semicircle in the medium frequency region, indicating lower R_{ct} value compared to cells based on alumina coated NMC622 (R_{ct} increasing with increasing coating thickness; highest for 10 nm Al_2O_3 on NMC622). This behavior is attributed to the low ionic and electronic conductivity of the alumina coating layer, which impedes Li^+ ttransport at the surface of NMC particles. Impedance in the high frequency region denoted by R_{CEI} is growing with cycling and shows the higher value for 5 nm compared to pristine and 10 nm alumina coated NMC622. However, the positive effect of coating is observed for R_{ct} after 200 charge/discharge cycles as shown in Figure 6b), where the cells based on alumina coated NMC622display a lower R_{ct} in the medium frequency region, probably due to the homogenous (de−) lithiation and formation of less resistive CEI. Whereas, R_{ct} is substantially higher for the pristine NMC622, which is in line with the more pronounced capacity fade for the pristine NMC622 and improved cycling stability for the alumina coated NMC622 (as shown in Figure 4b). Reduction in the impedance for the alumina coated NMC622 compared to pristine NMC622 can be explained as the alumina coating protects the CAM from reaction with the electrolyte which can improve structural stability and protect the positive active material against the chemical attack of HF preventing the formation of a resistive layer at the electrode interface, composed of inactive degradation products.[41] In summary, the results reveal that the alumina coating had no negative impact on the cell impedance after charge/discharge cycling, and the EIS results are in complete agreement with charge/discharge cycling data where the cells based on thinner coating (5 nm) show the highest capacity retention and the lowest cell impedance after 200 charge/discharge cycles.

2.3. Post mortem analysis

In order to understand the effects causing the electrochemical performance enhancement, *post mortem* analysis was performed for the electrochemically aged samples (200 cycles) using HR-TEM and STEM imaging, NBD, STEM-EDX and EELS. Figure 7 shows HR-TEM images, BF-STEM images, and NBD patterns of samples from electrodes based on the uncoated (pristine) and 10 nm alumina coated NMC622. Figure 7a) shows an area of a pristine NMC622 particle near the surface, which has undergone a phase transformation from a rhombohedral layered (R-3m) to the rock-salt (Fm-3m) phase, which was also confirmed by the NBD pattern acquired in [111] zone axis from the electrode surface (Figure 7c)). In the highly delithiated state due to local inhomogeneity, surface degradation in the presence of highly oxidized *TM* species leads to the transport and dissolution of *TMs*, formation of the rock-salt phase at the cathode surface, which is linked with the irreversible oxygen loss from the surface structure.[42] Anisotropic volume changes due to the phase transformation (phase with larger lattice parameters) in the highly delithiated state induces mechanical stress within the secondary particles, which if not compensated by the neighboring particles, eventually leads to particle cracking.[42] After 200 charge/discharge cycles, the BF-STEM image shows severe cracking of NMC622 particle and some parts, where the particle was partially disintegrated and formed voids in the structure, as shown in Figure 7b). Particle cracking leads to the loss of electronic contact between the particles and gives rise to enhanced polarization and detrimental side reactions due to the formation of new contact surfaces between the electrolyte and the active material, contributing to the degradation of performance and capacity. Surface degradation from the electrolyte attack is typically manifested by the rock salt phase formation at the cathode surface that raises the charge transfer resistance and hinders the Li^+ transport, which agrees with the EIS data. Due to the Li^+ concentration gradient formed during discharging, bulk particles are more likely to stay in the delithiated state than surface particles and are more susceptible to electrolyte penetration through micro-cracks causing more surface damage resulting in severe capacity fade.[43] Whereas for the electrodes based on alumina coated
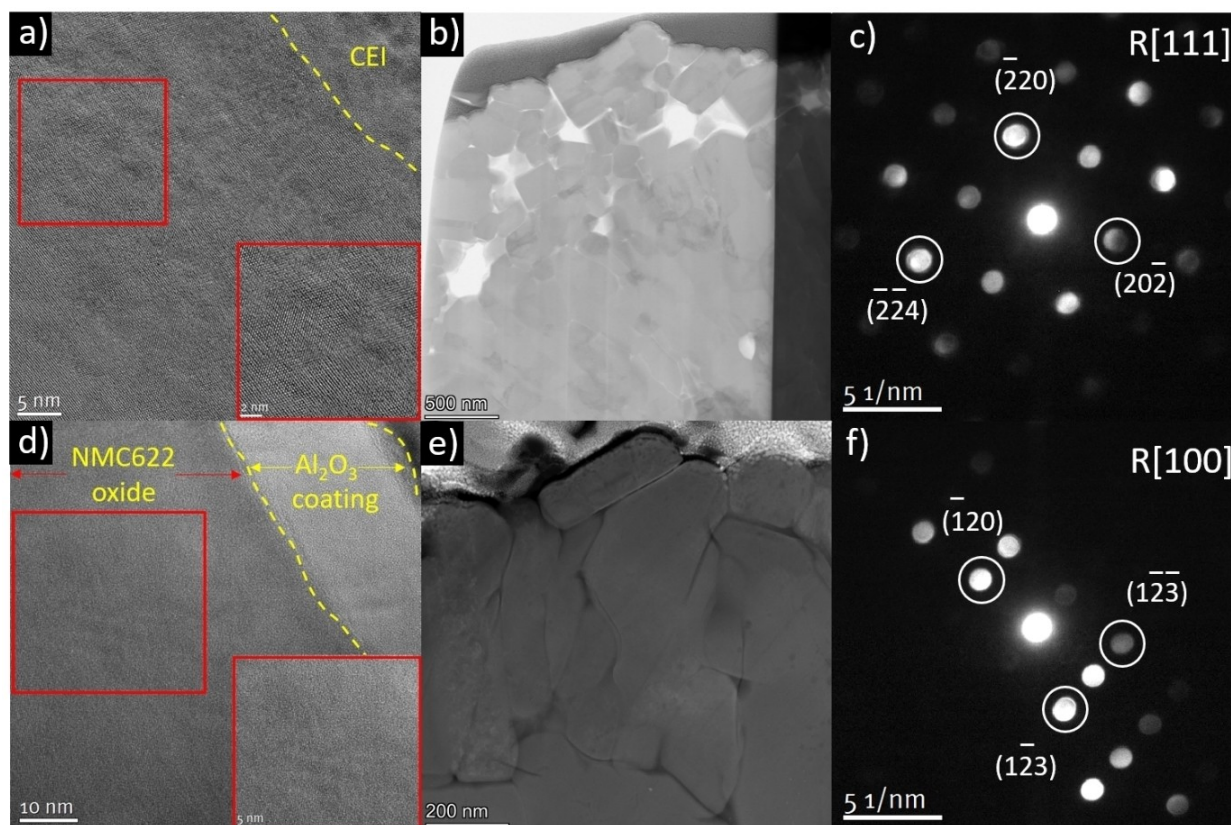
Batteries & Supercaps

Research Article
doi.org/10.1002/batt.202300580

Chemistry
Europe

European Chemical
Societies Publishing

Figure 7. HR-TEM image, BF-STEM image, and NBD pattern of (a, b, c) pristine and (d, e, f) 10 nm alumina coated NMC622 after 200 charge/discharge cycles.

NMC622, homogenous (de−)lithiation occurs due to the uniform CEI, suppressing the particle cracking and phase transformation. In Figure 7d) highlighted with the yellow dotted line, a very homogenous and thin alumina coating is visible, which is completely intact after 200 cycles and does not contain any cracks or pores. Underneath the coating layer, the surface structure of NMC622 did not show any phase transformation as seen with HR-TEM images (Figure 7d)). The layered structure was preserved and the particle cracking was suppressed because of the beneficial effect of the alumina coating (Figure 7e)). The NBD pattern acquired in [100] zone axis from the surface near to the alumina coating also shows that the layered structure was preserved by the coating layer during electrochemical cycling (Figure 7f). The alumina coating effectively protects the direct contact between the CAM and the electrolyte and facilitates homogenous (de−)lithiation hence, the degradation reactions were prevented, leading to enhanced electrochemical performance and reduced capacity fading.

In order to further understand the changes in the surface structure after 200 charge/discharge cycles, EELS analysis of the pristine and 10 nm alumina coated NMC622 based electrodes was performed in different regions from the surface to the bulk, as shown in Figure 8 (a and b). The fine structure and energy positions of O−K, Co−, Ni−, and Mn−L edges give information about the electronic structure of the sample and thus, the structural evolution can be studied for the cycled samples. Figure 8 (c and d) compares the EELS spectra of O−K and Mn−L

edges integrated from the surface and bulk of the pristine NMC622, where progressive changes were observed for the O−K edge. The peak at an energy loss value of 528 eV is referred to the O−K edge pre-peak in the literature, which associates with the transition of $1s$ electrons to the unoccupied O-$2p$ states hybridized with the TM-$3d$ states.[44] Therefore, the pre-peak observed in the bulk of pristine NMC622 diminished at the surface, as shown in Figure 8c), suggesting a change in the electronic environment of oxygen leading to oxygen vacancy formation, modification of TM-$3d$ orbitals, and change in the TM-TM bond length.[45] The changes in the TM bond length indicate the formation of a new phase (spinel/rock-salt) at the surface and can be further perceived by the Mn−L peaks.[46] The Mn−L peaks at the surface shift to lower energy loss values indicating a reduction of Mn (Mn^{4+} $vs.$ $Mn^{3.5+}$) due to oxygen release during prolonged charge/discharge cycling.[47] Since the average oxidation state of Mn is lower in the rock-salt phase than in the layered structure, the phase transformation from the layered to the rock-salt phase at the surface was confirmed. Moreover, an increase in intensity for the Mn-L_3 edge shows a surface enrichment upon charge/discharge cycling, which is consistent with the TEM results where the surface reconstruction was observed from the layered to the rock-salt phase. Furthermore, peaks for all transition metals were shifted toward lower energy loss values at the surface in comparison to the bulk, indicating an overall decrease in the
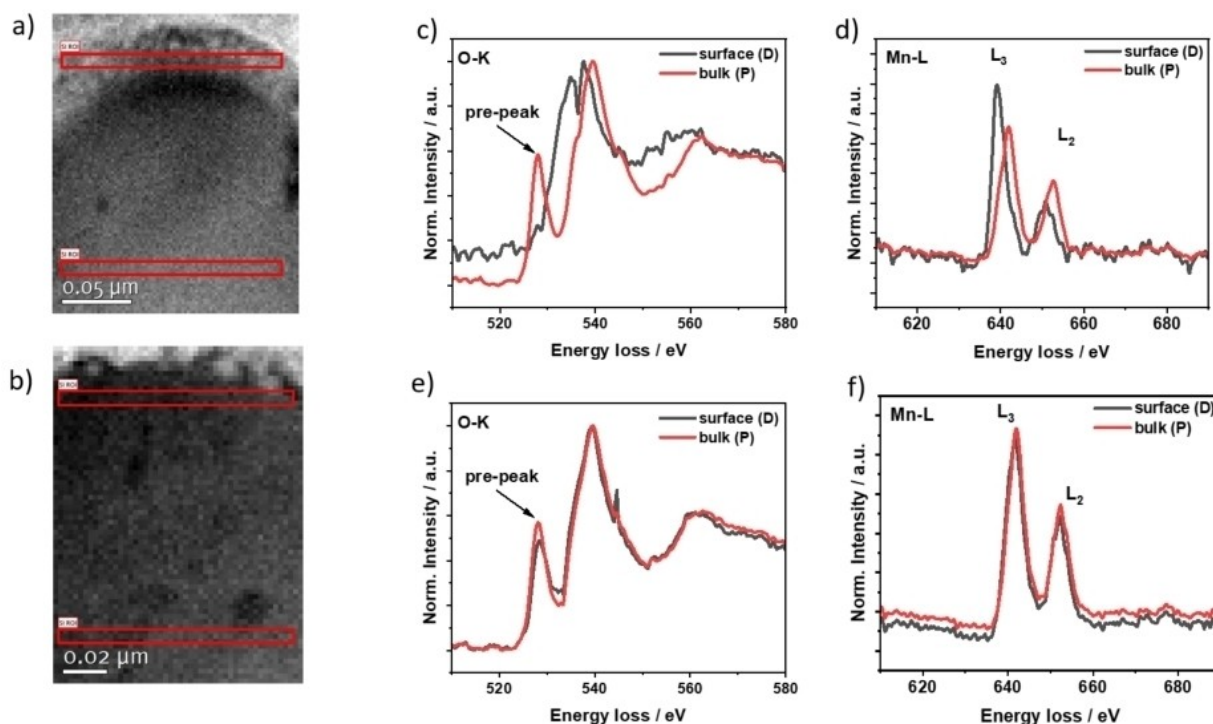
Batteries & Supercaps

Research Article
doi.org/10.1002/batt.202300580

Chemistry
Europe
European Chemical
Societies Publishing

Figure 8. Core-loss EELS-SI data of a) pristine NMC622 b) 10 nm alumina coated NMC622 (c, d) O–K edge and Mn–L edge for pristine, (e, f) O–K edge and Mn–L edge for 10 nm alumina coated NM622 after 200 charge/discharge cycles (EELS spectra integrated from the rectangles shown in a and b).

oxidation states of all *TM*s as shown in Figure 8d) and S3 (a and b).[48]

EELS spectra of the alumina coated NMC622 after cycling is shown in Figure 8 (e and f). The intensity of O–K edge peak and pre-peak integrated from the bulk and surface remained unchanged by charge/discharge cycling, indicating no change in the electronic environment of oxygen and formation of oxygen vacancies. Therefore, the layered structure of NMC622 was preserved at the surface and in the bulk as no phase transformation or surface reconstruction occurred for the alumina coated NMC622. Moreover, the peaks for *TMs* were similar in intensities and energy loss position at the surface and in the bulk, indicating no change in the oxidation states of *TMs*

due to more uniform (de–)lithiation that prevents phase transformation and particle cracking (Figure 8f) and S3 (c and d)).[49] Overall, the observations from the EELS and TEM analysis provide supporting evidence for the superior long-term cycling stability for the alumina-based coated samples and the continuous capacity fade for the uncoated samples induced by the surface degradation mechanism such as phase transformation leading to mechanical stress and particle cracking.

Beyond performance, the coating can also affect the CAM safety properties. Therefore, TGA was performed to determine the thermal stability of the electrodes based on pristine and alumina coated NMC622 in charged state after formation and 200 charge/discharge cycles. Figure 9a) shows the mass loss of
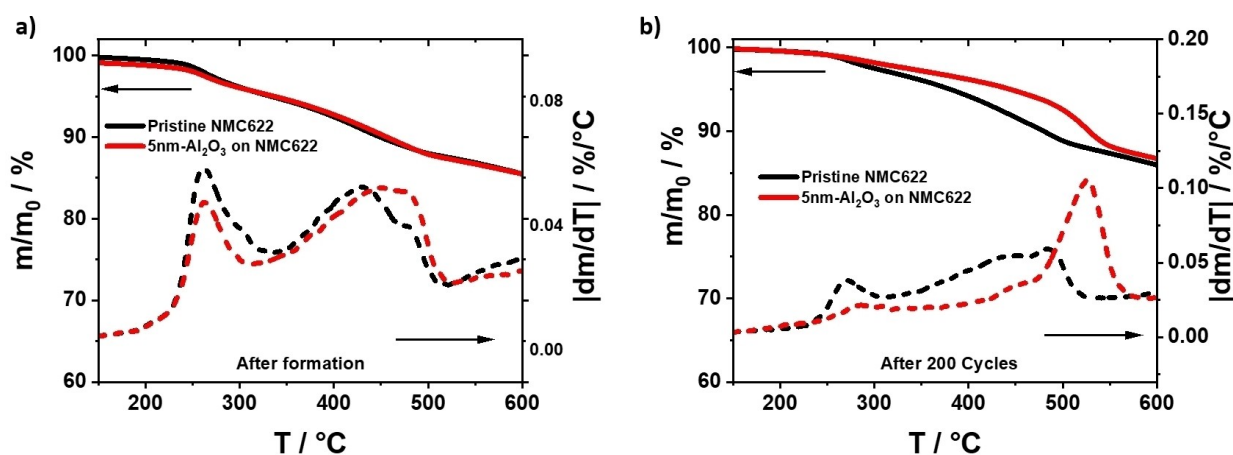

Figure 9. TGA of delithiated pristine and 5 nm alumina coated NMC622 electrodes charged to 4.3 V a) after formation and b) after 200 cycles.

Batteries & Supercaps

Research Article
doi.org/10.1002/batt.202300580

Chemistry
Europe

European Chemical
Societies Publishing

NMC622 based electrodes in the temperature range of 150 to 600 °C indicating a similar mass loss percentage for both the pristine and 5 nm alumina coated NMC622. The derivative of the mass loss is plotted with dotted lines indicating at which temperatures mass loss occurs so that each peak can be attributed to a specific thermal decomposition reaction. For NMC622 based electrodes after formation cycles, the first phase transition starts at 220 °C and is complete at 300 °C, which is attributed to the transformation from the layered structure to M_3O_4 (M=Mn, Ni, Co) spinel.[10] Moreover, phase transformation is directly linked with oxygen release, which is observed as moss loss in TGA. Oxygen release at low temperatures is a particularly safety determining factor in LIBs due to the strongly exothermic reaction of oxygen species released from the cathode, with the electrolyte that can cause serious safety problems like fire and explosion.[50] In the temperature range of 350 to 500 °C the phase transition from the M_3O_4 spinel to the rock-salt is completed and the pristine NMC622 completely transforms to rock-salt before 600 °C.[10] However, in addition to the phase transformation, the mass loss in the temperature range of 350 to 500 °C can be also attributed to the thermal decomposition of the PVdF binder.[42] Figure 9b) shows the TGA of the electrochemically aged electrodes based on pristine and 5 nm alumina coated NMC622. The onset temperature for thermal decomposition reactions is similar for both electrodes, but the pristine electrode shows a quite rapid mass loss compared to the alumina coated NMC622, which showed a delayed mass loss and the complete transformation from the layered to the rock-salt occurred at higher temperatures. First phase transformation is observed for the pristine NMC622 between 220 to 300 °C indicating a sudden oxygen release which can trigger a thermal runaway. In contrast, the peak intensity of the alumina coated NMC622 is quite low indicating a slow release of oxygen and retention of the layered structure until higher temperatures. For the alumina coated NMC622, sudden oxygen release is suppressed, pushing the oxygen release and mass loss to higher temperatures which is critical in improving the safety characteristics of LIBs.[10,50] Therefore, it is concluded that the alumina coating enables enhanced safety characteristics of the battery cell alongside an improvement in electrochemical performance, in particular after longer cycling.

3. Conclusions

In this study, an alumina coating with different thicknesses was deposited on NMC622 secondary particles using a novel technique, *i.e.* RF-magnetron sputtering. The coatings were found to be homogenous, displayed good surface coverage and the thicknesses achieved were close to the theoretically adjusted values. The surface coverage and homogeneity were confirmed using SEM, EDX, and STEM-EDX. SEM images showed no considerable change in surface morphology after the coating and EDX showed the presence of alumina coating on the NMC particles. STEM-EDX analysis also proved the homogeneity of the coating. In the rate capability analysis, pristine NMC622 outperformed alumina coated NMC622 and the cells based on

alumina coated NMC622 showed similar behavior up to 2C and only at 5C a difference in discharge capacity was observed regarding a decreasing rate performance with increasing coating thickness. Long-term charge/discharge cycling stability and capacity retention were investigated, where the coated samples performed remarkably better than the uncoated NMC622. The 5 nm alumina coated NMC622 showed 94% capacity retention and the pristine sample showed 81% capacity retention after 200 cycles. The improved electrochemical performance was attributed to the alumina coating protecting CAM against degradation effects and the formation of a stable Al_2O_3 based CEI leads to homogenous (de−)lithiation, that suppressed phase transformation, structural degradation and particle cracking, which were considered to be the main reason for the severe capacity fading of the pristine NMC622.

Post mortem analysis of the electrochemically aged electrodes based on pristine NMC622 *via* TEM showed particle cracking, and structural transformation from the layered to the rock-salt. The alumina coated NMC622 exhibited no signs of particle cracking and structural degradation reactions as the alumina coating layer successfully protected the CAM particles from the reaction with the electrolyte components. EELS analysis showed the absence of O−K pre-peak at the surface for the pristine electrodes, indicating loss of oxygen and vacancy formation. For pristine electrode the peaks for *TMs* were shifted to lower energy loss value, indicating the reduction of the oxidation states of *TMs*, confirming the phase transformation from the layered to the rock-salt phase. For the coated sample, the O−K pre-peak was present at the surface and no shift in the *TMs* peak was observed indicating the layered structure of NMC622 was intact after prolonged cycling. Furthermore, the alumina coating improved the thermal stability of NMC622 after charge/discharge cycling as the alumina coating delayed the first oxygen release and phase transformation to the rock-salt until higher temperatures, while the pristine sample suffered continuous oxygen loss and phase transformation due to enhanced degradation during the charge/discharge cycling.

Overall, the strategy of using magnetron sputtering on powders opens up a novel, effective and feasible path for interphase design using surface coatings for the active materials where a variety of coatings can be applied using this method. Improvement in the electrochemical performance of the alumina coated NMC622 can be ascribed to the effective protection of the cathode active material from direct contact with the electrolyte and mitigating the side reactions and hence preventing particle cracking and structural degradation, which in turn considerably enhances the cycling stability and capacity retention.

Experimental Section

Al₂O₃ coating with magnetron sputtering

Pristine, completely uncoated NMC622 was obtained from BASF as positive active material. Alumina-coated NMC was prepared by direct deposition of aluminum (Al) metal in oxygen atmosphere using magnetron sputtering. For Al_2O_3 coating, reactive sputtering

Batteries & Supercaps

Research Article
doi.org/10.1002/batt.202300580

Chemistry Europe
European Chemical
Societies Publishing

was performed using Argon (Argon 4.6; Westfalen AG) and oxygen (Oxygen 5.0, Westfalen AG). Base pressure of 10^{-5} mbar was obtained in the sputtering chamber, and then equal volume ratios of Ar and O_2 were introduced to adjust a working pressure of 10^{-3} mbar. First, the deposition rate of the Al-target (diameter: 6 inches, purity 99,99%; FHR) was estimated by depositing a thin film of Al in O_2 atmosphere on a silicon wafer (Siltronic CZ06n SSP, thickness 525 μm). The obtained coating thickness was determined using a thickness profilometer (Bruker DektakXT), and accordingly, the deposition rate per hour was calculated. The theoretical thickness of the coating on powder against time was estimated using the deposition rate on a silicon wafer with respect to time, area of target (A), the density of active material and target (ρ) as well as morphology and particle size of powder (r; corresponding equations 1, 2 and 3 are presented in the supplementary information). Three different theoretical coating thicknesses were applied: 5 nm, 7 nm and 10 nm, corresponding to wt%. of 0.0046, 0.0067 and 0.0094, respectively. The power of 600 W was applied to the magnetron source of the sputtering device for a calculated time to get the desired thickness of the coating. To ensure a homogeneous deposition of alumina coating on the NMC622 particle surfaces the sample holder was rotated at 20 rpm. Furthermore, two additional brushers and a roller were used (the 1st brush and roller moving parallel to each other mixing and pressing the powder to make sure no agglomerates are formed while the 2nd brush ensured the powder is not sticking to the sides of the sample holder), which were moving continuously throughout deposition to guarantee homogenous coating of the complete powder surface. The coating thickness was calculated by adjusting the deposition time of 2, 2.8 and 4 h corresponding to Al_2O_3 thickness of 5, 7 and 10 nm on NMC622 secondary particles.

Electrode preparation

Electrodes were prepared by mixing pristine or alumina coated NMC622 as active material, carbon black (SuperC65, Imerys Graphite & Carbon)) as conductive additive, Poly (vinylidene difluoride) (PVDF, Solef 5130, Solvay) as binder in a weight ratio of 95:2:3 and N-Methyl-2-pyrrolidone (NMP, anhydrous, purity: 99.5%, Sigma-Aldrich) was used as processing solvent. After the mixing process, the electrode paste was casted on aluminum foil (20 μm, Nippon foil, washed with ethanol prior to coating) using a doctor blade (Zehntner GmbH) and an automatic film applicator (Sheen Instruments). Afterwards, electrode sheets were dried in an atmospheric oven at 100 °C for 1 h and then calendered to a porosity of 35%. The graphite-based negative electrode was obtained from an in-house pilot battery line (recipe and procedure described elsewhere[51]). Electrodes were prepared with a diameter of 14 mm for cathodes and 15 mm for anodes and dried in a Büchi B-585 glass drying oven under reduced pressure ($<5\times10^{-2}$ bar) at 120 °C for 12 h. Active mass loading for positive electrodes was 12 mg cm^{-2}, corresponding to an areal capacity of 2.1 mAh cm^{-2} (175 mAh g^{-1} practical capacity). The areal capacity of the graphitic anode was 2.3 mAh cm^{-2}. For electrochemical investigation, electrode balancing of anode to cathode, N:P ratio was set to 1.1.

Material characterization

Particle morphology and the surface topography of electrodes, Al_2O_3 coating coverage and homogeneity, were investigated using scanning electron microscopy (SEM; Carl Zeiss AURIGA) at an acceleration voltage of 3 kV for NMC622 powders and electrodes surface analysis and 15 kV for EDX measurements. For the last mentioned technique EDX, an X–Max 80 mm^2 detector was used

and data evaluation was performed by INCA software (Oxford instrument).

HR-TEM, high-angle annular dark field (HAADF-STEM), annular bright field (ABF-STEM), energy dispersive X-ray spectroscopy (EDX-STEM), NBD pattern analyses, and EELS-STEM techniques were carried out using a FEI Titan Themis G3 300 transmission electron microscope (TEM) equipped with a monochromator, a Gatan Image Filter (GIF) quantum ER/965 P spectrometer, ultrafast dual EELS spectrum imaging (EELS-SI), Ceta 16 m camera, HAADF, DF, and ABF image detectors, and Super-X EDX detector. For all TEM measurements, an accelerating voltage of 300 kV was used. The EELS-SI was used to acquire the summed spectra over the selected area of interest. EELS spectra were recorded with 0.25 eV/channel dispersion and a drift corrector was used during EELS-SI acquisition. The background of EELS spectra was removed using a power law implemented in Gatan Digital Micrograph (DM3). The NBD spectrum image (NBD-SI) was acquired using a micro-probe mode with a semi-convergence angle of 1.0 mrad. The NBD-SI data analysis was performed using the custom DM plug-ins.[52] Since the electrode materials are beam sensitive, low electron beam current and low exposure time were used for acquiring EDX mapping, NBD-SI, and EELS-SI. The cycled cells were disassembled in the discharged state inside an Ar-filled glovebox for TEM investigation. For TEM sample preparation, the as-synthesized NMC622 powder was dispersed on a carbon-supported Cu-grid and cross-sectional TEM lamellae were prepared from the cycled electrodes using a focused ion beam / scanning electron microscope (FIB/SEM ZEISS cross-beam 340). A vacuum transfer holder (Gatan) was used for transferring the samples from the glove box into the TEM.

Cell preparation and electrochemical characterization

Electrochemical characterization of uncoated and alumina coated NMC622 based electrodes was carried out in a two-electrode CR2032 coin cell setup with lithium metal (Albemarle; Purity: Battery grade) NMC||Li and graphite NMC||C as anodes for rate capability and long-term charge/discharge cycling investigations, respectively. A polypropylene separator (Celgard 2500, 16 mm in diameter) was placed between two electrodes soaked with 50 μL electrolyte consisting of 1 M LiPF$_6$ in ethylene carbonate (EC) and ethyl methyl carbonate (EMC; 3:7 by weight) with 2% vinylene carbonate (VC) as an additive. Cells were assembled in a dry room atmosphere with a dew point below −50 °C and rested for 6 h before cycling.

Electrochemical charge/discharge cycling was performed using a Maccor Series 4000 battery tester (Maccor, Inc.) within the cell voltage range 2.8–4.3 V at 20 °C. Three formation cycles were performed at 0.1 C charge/discharge rate. Afterwards, C||NMC622 based cells were cycled at 1C (1C corresponding to 175 mA g^{-1}), and Li||NMC622 based cells were cycled at 0.1, 0.2, 0.5, 1, 2 and 5C with three cycles at each C-rate. At least three cells were evaluated for each study to ensure reproducibility. Electrochemical impedance spectroscopy (EIS) measurements were performed using a Solartron FRA 1260 frequency response analyzer combined with a Solartron model 1287 electrochemical interface. The spectra were collected in potentiostatic mode in the frequency range between 1 MHz and 20 mHz. 5 mV perturbation amplitude was applied for all cells. RelaxIS software from rhd Instruments GmbH & Co. KG, was used to evaluate the results and perform the equivalent circuit modeling.

Thermal analysis

For *post mortem* analysis, cyclic aged cells were opened in an Ar-filled glovebox and washed with dimethyl carbonate (DMC,

Batteries & Supercaps

Research Article
doi.org/10.1002/batt.202300580

Chemistry
Europe

European Chemical
Societies Publishing

anhydrous, purity: 99.5 %, Sigma-Aldrich) solution three times to remove electrolyte residues from the electrode surface. TGA was performed using a SDT IR Q500 from TA Instruments. 5 mm samples were punched from cyclic aged electrodes (200 cycles) and transferred in a platinum pan. The temperature was equilibrated at 30 °C for 40 min in an isothermal step with a helium balance flow rate of 30 mL min⁻¹ and mass flow of 10 mL min⁻¹. Measurements were performed with a heating rate of 5 K min⁻¹ up to 600 °C.

4. Supporting Information

Supporting information is available from the Wiley Libraray or from the author

Conflict of Interests

The authors declare no conflict of interest

Data Availability Statement

The data that support the findings of this study are available from the corresponding author upon reasonable request.

[1] Y. Nishi, *Chem. Rec.* **2001**, *1*, 406–413.
[2] J. M. Zheng, J. Li, Z. R. Zhang, X. J. Guo, Y. Yang, *Solid State Ionics* **2008**, *179*, 1794–1799.
[3] K. Mizushima, P. C. Jones, P. J. Wiseman, J. B. Goodenough, *Mater. Res. Bull.* **1980**, *15*, 783–789.
[4] Y. Arinicheva, M. Wolff, S. Lobe, C. Dellen, D. Fattakhova-Rohlfing, O. Guillon, D. Böhm, F. Zoller, R. Schmuch, J. Li, M. Winter, E. Adamczyk, V. Pralong in *Advanced ceramics for energy conversion and storage, Elsevier series on advanced ceramic materials*; (Ed. O. Guillon), Elsevier, Amsterdam, **2019**, pp. 549–709.
[5] D. Becker, M. Börner, R. Nölle, M. Diehl, S. Klein, U. Rodehorst, R. Schmuch, M. Winter, T. Placke, *ACS Appl. Mater. Interfaces* **2019**, *11*, 18404–18414.
[6] R. S. Negi, S. P. Culver, A. Mazilkin, T. Brezesinski, M. T. Elm, *ACS Appl. Mater. Interfaces* **2020**, *12*, 31392–31400.
[7] J. Vetter, P. Novák, M. R. Wagner, C. Veit, K.-C. Möller, J. O. Besenhard, M. Winter, M. Wohlfahrt-Mehrens, C. Vogler, A. Hammouche, *J. Power Sources* **2005**, *147*, 269–281.
[8] S.-K. Jung, H. Gwon, J. Hong, K.-Y. Park, D.-H. Seo, H. Kim, J. Hyun, W. Yang, K. Kang, *Adv. Energy Mater.* **2014**, *4*, 1300787.
[9] B. Ji, F. Zhang, M. Sheng, X. Tong, Y. Tang, *Adv. Mater.* **2017**, *29*.
[10] S.-M. Bak, E. Hu, Y. Zhou, X. Yu, S. D. Senanayake, S.-J. Cho, K.-B. Kim, K. Y. Chung, X.-Q. Yang, K.-W. Nam, *ACS Appl. Mater. Interfaces* **2014**, *6*, 22594–22601.
[11] J. Kasnatscheew, S. Röser, M. Börner, M. Winter, *ACS Appl. Energ. Mater.* **2019**, *2*, 7733–7737.
[12] Y. Su, L. Li, G. Chen, L. Chen, N. Li, Y. Lu, L. Bao, S. Chen, F. Wu, *Chin. J. Chem.* **2021**, *39*, 189–198.
[13] W. Liu, P. Oh, X. Liu, M.-J. Lee, W. Cho, S. Chae, Y. Kim, J. Cho, *Angew. Chem. Int. Ed.* **2015**, *54*, 4440–4457.
[14] D. R. Gallus, R. Wagner, S. Wiemers-Meyer, M. Winter, I. Cekic-Laskovic, *Electrochim. Acta* **2015**, *184*, 410–416.
[15] X. Tan, M. Zhang, J. Li, D. Zhang, Y. Yan, Z. Li, *Ceram. Int.* **2020**, *46*, 21888–21901.
[16] D. Weber, Đ. Tripković, K. Kretschmer, M. Bianchini, T. Brezesinski, *Eur. J. Inorg. Chem.* **2020**, *2020*, 3117–3130.
[17] U. Nisar, N. Muralidharan, R. Essehli, R. Amin, I. Belharouak, *Energy Storage Mater.* **2021**, *38*, 309–328.
[18] R. S. Negi, E. Celik, R. Pan, R. Stäglich, J. Senker, M. T. Elm, *ACS Appl. Energ. Mater.* **2021**, *4*, 3369–3380.
[19] S. Hildebrand, C. Vollmer, M. Winter, F. M. Schappacher, *J. Electrochem. Soc.* **2017**, *164*, A2190-A2198.
[20] M. J. Herzog, D. Esken, J. Janek, *Batteries & Supercaps* **2021**, *4*, 1003–1017.
[21] W. Zhang, L. Liang, F. Zhao, Y. Liu, L. Hou, C. Yuan, *Electrochim. Acta* **2020**, *340*, 135871.
[22] B. Xiao, B. Wang, J. Liu, K. Kaliyappan, Q. Sun, Y. Liu, G. Dadheech, M. P. Balogh, L. Yang, T.-K. Sham, R. Li, M. Cai, X. Sun, *Nano Energy* **2017**, *34*, 120–130.
[23] E. Adhitama, S. van Wickeren, K. Neuhaus, L. Frankenstein, F. Demelash, A. Javed, L. Haneke, S. Nowak, M. Winter, A. Gomez-Martin, T. Placke, *Adv. Energy Mater.* **2022**, 2201859.
[24] X. Xiong, Z. Wang, X. Yin, H. Guo, X. Li, *Mater. Lett.* **2013**, *110*, 4–9.
[25] Y. Cao, X. Qi, K. Hu, Y. Wang, Z. Gan, Y. Li, G. Hu, Z. Peng, K. Du, *ACS Appl. Mater. Interfaces* **2018**, *10*, 18270–18280.
[26] Z. Chen, Y. Qin, K. Amine, Y.-K. Sun, *J. Mater. Chem.* **2010**, *20*, 7606.
[27] A. Zhou, Q. Liu, Y. Wang, W. Wang, X. Yao, W. Hu, L. Zhang, X. Yu, J. Li, H. Li, *J. Mater. Chem. A* **2017**, *5*, 24361–24370.
[28] D. Mohanty, K. Dahlberg, D. M. King, L. A. David, A. S. Sefat, D. L. Wood, C. Daniel, S. Dhar, V. Mahajan, M. Lee, F. Albano, *Sci. Rep.* **2016**, *6*, 1–16.
[29] K. Yoo, Y. Kang, K. Im, C.-S. Kim, *Materials* **2017**, *10*, 1273.
[30] B. Mukherjee, N. Ravishankar, *Nanotechnology* **2006**, *18*, 25603.
[31] R. Pfeffer, R. N. Dave, D. Wei, M. Ramlakhan, *Powder Technol.* **2001**, *117*, 40–67.
[32] M. J. Herzog, N. Gauquelin, D. Esken, J. Verbeeck, J. Janek, *ACS Appl. Energ. Mater.* **2021**, *4*, 8832–8848.
[33] A. M. Wise, C. Ban, J. N. Weker, S. Misra, A. S. Cavanagh, Z. Wu, Z. Li, M. S. Whittingham, K. Xu, S. M. George, M. F. Toney, *Chem. Mater.* **2015**, *27*, 6146–6154.
[34] G. Dai, G. Yu, F. Shen, J. Cao, L. Ni, Y. Chen, Y. Tang, Y. Chen, *Ionics* **2016**, *22*, 2021–2026.
[35] Y. Kim, H. S. Kim, S. W. Martin, *Electrochim. Acta* **2006**, *52*, 1316–1322.
[36] Y. Shi, M. Zhang, D. Qian, Y. S. Meng, *Electrochim. Acta* **2016**, *203*, 154–161.
[37] J. L. Tebbe, A. M. Holder, C. B. Musgrave, *ACS Appl. Mater. Interfaces* **2015**, *7*, 24265–24278.
[38] W. Liu, P. Oh, X. Liu, S. Myeong, W. Cho, J. Cho, *Adv. Energy Mater.* **2015**, *5*, 1500274.
[39] A. Friesen, X. Mönnighoff, M. Börner, J. Haetge, F. M. Schappacher, M. Winter, *J. Power Sources* **2017**, *342*, 88–97.
[40] S. M. M. Alavi, C. R. Birkl, D. A. Howey, *J. Power Sources* **2015**, *288*, 345–352.
[41] C. Qin, J. Cao, J. Chen, G. Dai, T. Wu, Y. Chen, Y. Tang, A. Li, Y. Chen, *Dalton Trans.* **2016**, *45*, 9669–9675.

Batteries & Supercaps

Research Article
doi.org/10.1002/batt.202300580

Chemistry Europe
European Chemical
Societies Publishing

[42] M. Börner, F. Horsthemke, F. Kollmer, S. Haseloff, A. Friesen, P. Niehoff, S. Nowak, M. Winter, F. M. Schappacher, *J. Power Sources* **2016**, *335*, 45–55.

[43] H.-H. Ryu, K.-J. Park, C. S. Yoon, Y.-K. Sun, *Chem. Mater.* **2018**, *30*, 1155–1163.

[44] J. Graetz, C. C. Ahn, R. Yazami, B. Fultz, *J. Phys. Chem. B* **2003**, *107*, 2887–2891.

[45] D. Qian, B. Xu, M. Chi, Y. S. Meng, *Phys. Chem. Chem. Phys.* **2014**, *16*, 14665–14668.

[46] B. Xu, C. R. Fell, M. Chi, Y. S. Meng, *Energy Environ. Sci.* **2011**, *4*, 2223.

[47] H. Tan, J. Verbeeck, A. Abakumov, G. van Tendeloo, *Ultramicroscopy* **2012**, *116*, 24–33.

[48] L. David, K. Dahlberg, D. Mohanty, R. E. Ruther, A. Huq, M. Chi, S. J. An, C. Mao, D. M. King, L. Stevenson, D. L. Wood, *ACS Appl. Energ. Mater.* **2019**, *2*, 1308–1313.

[49] Y. Wu, C. Ma, J. Yang, Z. Li, L. F. Allard, C. Liang, M. Chi, *J. Mater. Chem. A* **2015**, *3*, 5385–5391.

[50] S.-M. Bak, K.-W. Nam, W. Chang, X. Yu, E. Hu, S. Hwang, E. A. Stach, K.-B. Kim, K. Y. Chung, X.-Q. Yang, *Chem. Mater.* **2013**, *25*, 337–351.

[51] S. Klein, P. Harte, J. Henschel, P. Bärmann, K. Borzutzki, T. Beuse, S. Wickeren, B. Heidrich, J. Kasnatscheew, S. Nowak, M. Winter, T. Placke, *Adv. Energy Mater.* **2021**, *11*, 2003756.

[52] C. Gammer, V. Burak Ozdol, C. H. Liebscher, A. M. Minor, *Ultramicroscopy* **2015**, *155*, 1–10.